# Journal Pre-proof


## Measurement of plastic strain and plastic strain rate during orthogonal cutting for Ti-6Al-4V

A. Sela, G. Ortiz-de-Zarate, D. Soler, G. Germain, P. Aristimuño, P.J. Arrazola

PII: S0020-7403(21)00132-6
DOI: https://doi.org/10.1016/j.ijmecsci.2021.106397
Reference: MS 106397

To appear in: *International Journal of Mechanical Sciences*

Received date: 22 September 2020
Revised date: 8 March 2021
Accepted date: 13 March 2021

Please cite this article as: A. Sela, G. Ortiz-de-Zarate, D. Soler, G. Germain, P. Aristimuño, P.J. Arrazola, Measurement of plastic strain and plastic strain rate during orthogonal cutting for Ti-6Al-4V, *International Journal of Mechanical Sciences* (2021), doi: https://doi.org/10.1016/j.ijmecsci.2021.106397

**Highlights**

- A methodology to measure strain and strain rate during orthogonal cutting is shown.
- The mathematical method uses a single picture of a deformed microgrid.
- The method was used with Ti-6Al-4V under plane strain condition.
- Obtained values are compared with literature, analytical, FEM and DIC results.

## Graphical Abstract

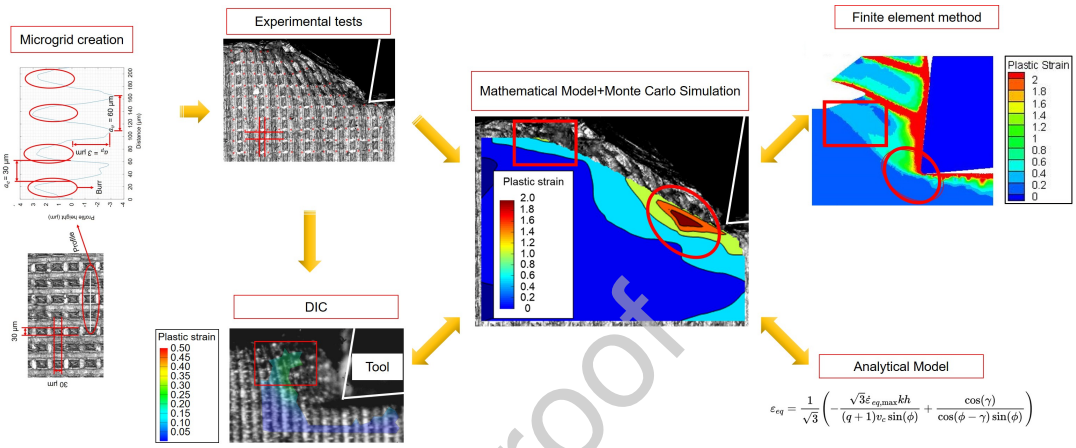

# Measurement of plastic strain and plastic strain rate during orthogonal cutting for Ti-6Al-4V

A. Sela[a,*], G. Ortiz-de-Zarate[a], D. Soler[a], G. Germain[b], P. Aristimuo[a], P.J. Arrazola[a]

[a] *Faculty of Engineering, Mondragon Unibertsitatea, 20500 Arrasate, Spain*
[b] *Arts et Mtiers Campus d'Angers, LAMPA EA1427, 2 bd du Ronceray, 49000 Angers, France*

**Abstract**

Finite Element Modelling used to predict machining outcomes needs to be supplied with the appropriate material thermomechanical properties which are obtained by specific testing devices and methodologies. However, these tests are usually not representative of the extreme conditions achieved in machining processes and the obtained material law may not be suitable enough. Inverse identification could address this problem by obtaining material thermomechanical properties directly from machining outcomes such as cutting forces, temperatures, strain or strain rates. Nevertheless, this technique needs to be supplied with accurate machining outcomes. However, some of them such as strain or strain rate are difficult to be properly measured. The aim of this paper is to present a methodology to measure plastic strain and strain rate during orthogonal machining under plane strain conditions. The main idea is to create a physical microgrid in a workpiece and to analyze the distortion suffered by this grid. The novelty of the method consists on its capability of measuring strain and strain rate fields in a very localized area (primary shear zone) using a single image. The methodology was applied in orthogonal cutting of Ti-6Al-4V under cutting conditions that are representative of the broaching process. Experimental results were compared with DIC measurements, analytical results based on unequal division shear zone model, literature results and with numerical fields obtained from an AdvantEdge-2D model.

*Keywords:* plastic strain, DIC, grid distortion, broaching, Ti-6Al-4V

## 1. Introduction

Machining remains one of the most relevant manufacturing operations in terms of volume and expenditure. Reliable models to simulate machining operations could be used to reduce costs and time facilitating proper tool and cutting

*Corresponding author:
*Email address:* asela@mondragon.edu (A. Sela)

conditions selection. Consistent input parameters such as material behaviour laws or tool-friction models are needed [1]. Among all workpiece materials, titanium alloys and, especially, alloy Ti-6Al-4V, which represents 50% of all titanium production [2] are widely used for medical, aeronautical and automotive applications, due to their low density, combined with strength at elevated temperatures and corrosion resistance [3]. Nevertheless, Ti-6Al-4V is known as a difficult-to-cut material as it tends to generate chip adhesion and segmentation because of its low thermal conductivity and chemical activity [3, 4]. Chip segmentation is a key aspect of machining, as it affects tool wear and surface integrity [5, 6] and makes it difficult to measure strain and strain rate. Contrary to what happens with continuous chips, the strain rate is notably variable during the machining process.

Material behaviour laws are obtained by carrying out thermomechanical characterization to determine the dependence of stresses with strain, strain rate and temperature. Thermomechanical tests are usually far different from real conditions achieved during machining, characterized by high temperatures, strain and strain rates in a low volume of material. For instance, Gleeble machines, usually used for material and damage characterization, are not able to reproduce the strain rates that take place during the machining process, especially using typical cylindrical samples [7]. Some specific samples are being developed trying to reproduce machining conditions in Gleeble machines [8], like hat samples used in [9, 10], reaching strain rates close to 1000 $s^{-1}$. Another possibility is the use of split Hopkinson bars (SPHB) to achieve higher strain rates. However, as stated in [11], achieved strains and heat rates are not representative of the machining process. In addition, all these tests are far from reproducing the extreme temperature rise, estimated at $10^4$ K/s, that the material suffers during the cutting process, which can cause the material behaviour to change [12].

Trying to overcome these limitations, material characterization can also be carried out using inverse simulation [13, 14]. In short, this technique recalculates the material parameters based on the experimental values obtained from real machining tests according to a predefined objective function [15, 16]. Material parameters are needed as reference to initialize the algorithm. Outputs such as cutting forces, chip geometry, tool-chip contact length [17, 18] and, in a few cases, cutting temperature [19], are usually considered, neglecting important outputs such as strain or strain rate, due to the lack of experimental data available. Direct measurement of plastic strain and strain rate in metal cutting is still a challenge [20]. To solve this problem, some solutions appear in literature, such as digital image correlation, particle image velocimetry and grid distortion.

Digital image correlation (DIC) is a non-contact method which allows the plastic strain to be determined by correlating two images of the same workpiece where a random speckle pattern was created, one deformed and the other undeformed [21]. The accuracy of the method is strongly dependent on how the random pattern was created (subset size, speckle size) [22, 23]. In machining operations, Baizeau et al. [24] studied different ways of creating the pattern, comparing etched or blasted specimens with different pressures. Thimm et al.

[25] used digital image correlation to carry out inverse simulation at high cutting speeds (up to 160 m/min). The inverse calculus is based on Oxley theory and limited to processes with continuous chips. Zhang et al. [14] carried out a similar analysis but at lower cutting speeds. Under these cutting conditions, they assumed that temperature and strain rate effects could be neglected to optimize the Johnson-Cook material parameters. There are few more publications on the topic (see for instance, [26, 27]), but this is still under investigation, and, to the best of our knowledge, the cutting conditions tested are usually far from the real ones achieved in machining.

The particle image velocimetry (PIV) is a technique which computes the velocity field by tracking the motion of different particles and then this field is used to determine strain and strain rates. For the specific case of machining, these particles are asperities created on the surface. However, to the best of our knowledge, this technique is still limited to very low cutting speeds, usually lower than 1 m/min (some examples can be seen in [28, 29]).

The limitations of DIC/PIV techniques usually to low cutting speeds and, especially, continuous chips (conditions tested in literature) are due to technical limitations rather than the technique itself. For this reason, these techniques are still under investigation for machining. In general, higher cutting speeds imply no enough illumination, no enough spatial resolution and decorrelation problems. In order to catch the process at higher cutting speeds, higher frame rates are needed (which means lower fields of view). However, recently, Harzallah et al. [30] published an interesting work in which the microstructure of the workpiece material was employed as random speckle pattern for Ti-6Al-4V, avoiding decorrelation problems. Furthermore, Zhang et al. [20] used a mechanical pattern for the same purpose. Another big drawback of these techniques lies in the fact that measurements can not be done under plane strain conditions typical of the orthogonal cutting process.

The strain of a surface can also be obtained by measuring the deformation suffered by a grid [31], usually comparing two images of the undeformed and the deformed grid, similar to the measurement protocol followed for DIC measurements. The accuracy of the method is highly conditioned by grid spatial resolution. There are different ways to generate the grid, as electron-litographic technique [32], photo-resist methods [33], mechanical methods [31] or laser printing [34]. The use of grids is not new and it is widely accepted for measuring strains in mechanical processes. Since the grids are engraved to the workpiece they will undergo the same deformation as the workpiece material. However, this technique is usually not applied in very aggressive conditions. In addition, although it was employed by different researchers, it was used for materials which tend to create continuous chips [32, 34, 35]. To the best of our knowledge, for other important materials in industry such as titanium alloys, this technique has not been employed yet. In addition, measurement techniques are based on the visible part of the workpiece which can be assumed to be close to plane stress conditions rather than plane strain. Therefore, the strains measured could not be representative of the orthogonal cutting process.

**Nomenclature**

| | |
|---|---|
| $v_C$ [m/min] | Cutting speed |
| $V_{AB}$,$V_{CD}$ [m/min] | Speed of an undeformed and a deformed segment |
| $L_{AB}$,$L_{CD}$ [mm] | Length of an undeformed and a deformed segment |
| $V_x$,$V_y$ [m/min] | Speed in x and y directions |
| $\dot{\varepsilon}_{xx}$ [$s^{-1}$] | Strain rate in x direction |
| $\dot{\varepsilon}_{yy}$ [$s^{-1}$] | Strain rate in y direction |
| $\dot{\gamma}_{xy}$ [$s^{-1}$] | Shear strain rate |
| $\dot{\varepsilon}_{eq}$ [$s^{-1}$] | Equivalent strain rate |
| $\varepsilon_{eq}$ [-] | Equivalent plastic strain |
| $a_e$ [$\mu m$] | Width of the straight path |
| $a_p$ [$\mu m$] | Axial depth of cut in micromilling |
| $a_v$ [$\mu m$] | Distance between two straight paths |
| $r$ [$\mu m$] | Ball end mill radius |
| $\sigma_x$ [$\mu m$] | Standard deviation in x direction |
| $\sigma_y$ [$\mu m$] | Standard deviation in y direction |
| $\gamma$ [°] | Rake angle |
| $\alpha$ [°] | Clearance angle |
| $r_e$ [$\mu$m] | Edge radius |
| $f$ [mm] | Uncut chip thickness (feed) |
| $w$ [mm] | Width of cut |
| $F_c$,$F_f$ [N/mm] | Cutting and feed force per millimetre of width of cut |
| $q, k$ [-] | Analytical model parameters |
| $\phi$ [°] | Shear angle |
| $t$ [mm] | Shear zone thickness |
| $L_c$ [mm] | Tool-chip contact length |

To sum up, reliable experimental data are needed to validate and optimize numerical models in order to reduce costs associated with the selection of tool and cutting conditions. Amongst all the outcomes, equivalent plastic strain and strain rate are some of the most difficult to measure under real machining conditions because of the severe conditions reached during the machining process. In this paper, in section 2, a method to determine the plastic strain and strain rate is proposed which is based only on one picture of the deformed grid, avoiding decorrelation problems usually associated with DIC/PIV techniques. Moreover, the set-up was designed to measure strain and strain rates under plane strain conditions, closer to the ones which represent orthogonal cutting processes. The uncertainty of this method was checked using a Monte Carlo simulation [36, 37].

In section 3 the experimental set-up is explained. Then, the experimental values of strain and strain rate obtained with the proposed methodology are presented and compared in section 5, with experimental values obtained from DIC measurements, analytical values obtained with the unequal division shear zone model as shows [38, 39], literature results given by Harzallah et al. in [30]and with the numerical outcomes reported by a validated finite element model of the chip formation process. The model employed was validated according to cutting forces, chip thickness, shear angle and tool chip contact length measurements,

as is shown in Appendix A.

## 2. Methodology

This section is divided into three subsections: in the first, the analytical method to measure the equivalent strain rate and plastic strain is explained. In the second, the procedure followed to create the mechanical grid is shown. Finally, the Monte Carlo method used to estimate the uncertainty is discussed.

### *2.1. Mathematical model*

To compute equivalent strain rates from a picture of a deformed grid a steady state flow is assumed. Moreover, considering that vertical displacements of the points of the non-deformed region are negligible, the horizontal grid lines represent streamlines (see Figure 1). Therefore, using the coordinates of the grid points, the length and the angle of each segment can be computed.

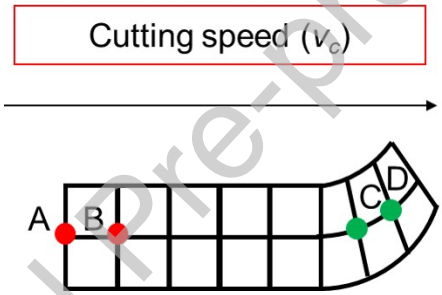


Figure 1: Steady flow assumption, AD curve represents a streamline.

Steady flow ensures that the time spent by the workpiece on travelling from A to B (an undeformed segment), was the same as for going from C to D (any deformed segment). A straightforward calculation allows the computation of the speed of the deformed segment CD ($V_{CD}$) with equation (1).

$$V_{CD} = V_{AB}\left(\frac{L_{CD}}{L_{AB}}\right) \tag{1}$$

where $V_{CD}$ is the speed of the deformed segment, $V_{AB}$ is the speed of the undeformed segment, $L_{CD}$ is the length of the deformed segment and $L_{AB}$ is the length of the undeformed segment.

Taking into account that AB segment was chosen far enough from the shear zone it can be assumed that the undeformed segment travels at the cutting speed, i.e. $V_{AB} = v_c$. The real speed was validated through high speed imaging. Using the inclination angle of each deformed segment, the velocity of each grid point could be decomposed ($V_x$, $V_y$). A biharmonic interpolation [40] is then used to estimate velocity fields, and those are used to perform numerical derivatives of $V_x$ and $V_y$.

According to Guo et al. [29], assuming small displacement hypothesis, the strain rate components can be calculated by equations (2), (3) and (4).

$$\dot{\varepsilon}_{xx} = \frac{dV_x}{dx} \tag{2}$$

$$\dot{\varepsilon}_{yy} = \frac{dV_y}{dy} \tag{3}$$

$$\dot{\gamma}_{xy} = \frac{dV_x}{dy} + \frac{dV_y}{dx} \tag{4}$$

where $\dot{\varepsilon}_{xx}$ represents the strain rate at the end of the segment in horizontal direction, $\dot{\varepsilon}_{yy}$ the strain rate at the end of the segment in vertical direction and $\dot{\gamma}_{xy}$ is the shear strain rate. With these components, the equivalent strain rate is calculated by equation (5), according to Von Mises criterion.

$$\dot{\varepsilon}_{eq} = \sqrt{\frac{4}{9}\left(\frac{1}{2}\left[(\dot{\varepsilon}_{xx} - \dot{\varepsilon}_{yy})^2 + \dot{\varepsilon}_{xx}^2 + \dot{\varepsilon}_{yy}^2\right] + \frac{3}{4}\dot{\gamma}_{xy}^2\right)} \tag{5}$$

Once the strain rate has been obtained, the equivalent plastic strain is calculated by integrating the strain rate along each streamline according to equation 6.

$$\varepsilon_{eq} = \left[\oint \dot{\varepsilon}_{eq} dt\right]_{streamline} \tag{6}$$

*2.2. Microgrid creation*

To perform the grid a Kern Evo Machine with a microball end mill with HARDMAX coating and a nominal radius of 50 $\mu$m (HSB 2001-0010) were used. To ensure a good microgrid quality it is important to guarantee a good surface roughness of the sample face where the grid is to be built. For this reason, before performing the grid, the surface was face-milled obtaining a Ra of 1.4 $\mu$m measured with a Mitutoyo roughness tester.

The created microgrid was formed by orthogonal straight paths (each one with a width ($a_e$) of 30 $\mu$m) placed every 60 $\mu$m (distance between two straight paths, $a_v$), see Figure 2. To determine the depth of cut $a_p$, equation 7 was used.

$$a_p = r - \frac{1}{2}\sqrt{4r^2 - a_e^2} \tag{7}$$

where $r$ is the radius of the ball end mill, obtaining a theoretical value of 2.3 $\mu$m. However, it is worth noting that $a_v$ is very sensitive to $a_p$ (especially at very low depths of cut) so this parameter must be properly controlled.

The depth of cut, $a_p$, was set to 2.5 $\mu$m, the real depth of cut being between 2 and 3 $\mu$m, taking into consideration thermal expansion and vibrations [41]. Therefore, according to equation 7, values of $a_e$ between 28 and 35 $\mu$m would be obtained. Nevertheless, as it could be seen in Figure 2b, the peak to valley

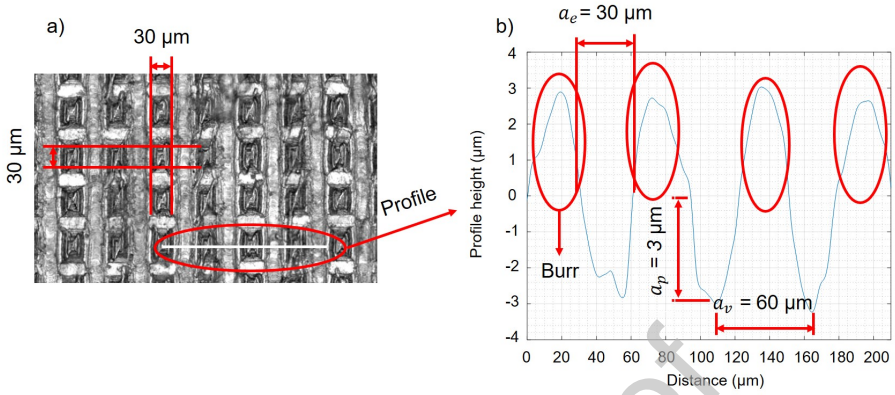


Figure 2: a) Undeformed grid measured using Alicona profilometer IFG4 with a magnification of 50X; b) Roughness profile from Alicona profilometer IFG4.

height was about 6 $\mu$m because of burring effects. However, this issue does not influence grid performance as Figure 2a shows. A set of 20 grids were created and measured using the Alicona profilometer. Based on these measurements, the dimensions of the grid were 30x30 $\mu$m with a standard deviation of $\pm$ 2 $\mu$m.

### *2.3. Uncertainty estimation of measurements using Monte Carlo simulation*

The uncertainty of the measurements is given in accordance with the *Guide to the Expression of Uncertainty in Measurement* GUM [42], using in all cases a coverage factor of 2.

As shown in section 2.1 the measurement method depends on the length $L_0$ of an undeformed segment of the grid ($L_{AB}$ in Figure 1). This length, taking into consideration equipment resolution and statistical methods, is around 60.56 $\mu$m with a standard uncertainty of $u_{L_0} = 0.05$ $\mu$m.

The measurement method is strongly conditioned by the grid coordinates of the region of interest (ROI) used to calculate the length of the deformed segments of the grid. At the present time, this set of coordinates is selected by a researcher by clicking on a picture of a deformed grid obtained with the Alicona profilometer IFG4, see for instance Figure 3.

In order to evaluate measurement uncertainty, the points selected by the researcher are disturbed using a two Gaussian distribution with a standard deviation of $\sigma_x = 1.2$ $\mu m$ and $\sigma_y = 1.4$ $\mu m$ in $X$ and $Y$ axis, respectively. These standard deviations were determined after taking the standard deviations of a sample of more than 10 repeated measurements into consideration. The new set of coordinates was then used to recalculate physical parameters explained in section 2.1. The equivalent plastic strain and equivalent strain rate fields reported in section 4 correspond to the most probable maximum strain rate in the region of interest, after performing more than 50000 iterations of Monte Carlo simulation of the grid points. The extended uncertainty is computed

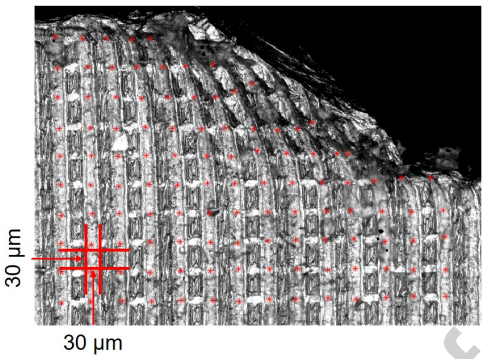


Figure 3: Image of grid state after machining at $v_c = 7.5$ m/min and $f = 0.4$ mm, where grid points are selected.

based on the variation of the maximum value of each field at each iteration, reporting an uncertainty of 15%.

The inclination angle of the horizontal line of the undeformed grid with respect to the $X$ axis, which was $0.020 \pm 0.002$ rad, could be considered an extra source of uncertainty. However, its influence on equivalent strain and strain rate uncertainty was proven to be negligible.

## 3. Experimental set-up

To implement the method exposed above, the set of linear orthogonal cutting tests showed in Table 1 was carried out on a Lagun CNC Milling center (CNC 8070). During the tests, cutting and feed forces were measured using a Kistler 9129AA dynamometer. The Kistler signal was synchronized with the high speed camera (Photron Fastcam APX-RS 250K) which recorded the machining process at 9000 frames per second. Therefore, the sampling rate was to 9000 Hz, which is assumed to be enough to reproduce the dynamics of the process as the oscillation frequency of cutting forces was observed to be notably lower. The tool holder was set in the spindle whereas the workpiece was fixed to the dynamometer clamped to the table. The scheme of the set-up is shown in Figure 4. See [43] for a more detailed description.

One of the main problems in ensuring orthogonal cutting conditions is to prevent the side flow (the lateral expansion of the non-constrained face due to machining process) which could lead to measure smaller values of strain and strain rate in the cutting plane [32]. Therefore, to measure plastic strain and strain rate under plane strain conditions, a grid was created on both sides of a workpiece (see Figure 5). This workpiece was clamped to a second workpiece, of the same material and same width (in the present case, 2 mm). This second workpiece was clamped to the dynamometer with the help of two screws as Figure 5a shows. Both workpieces were subjected to the machining process, the total width of cut being 4 mm. The clamping device shown in Figure 5a keeps

Table 1: Experimental plan for strain rate measurement using grid distortion on Ti-6Al-4V

| | | |
|---|---|---|
| Tool | Reference | TPUN 160308 |
| | Rake angle, $\gamma$ [°] | 6 |
| | Clearance angle, $\alpha$ [°] | 5 |
| | Edge radius, $r_e$ [$\mu$m] | 25 |
| | Coating | Nothing |
| Workpiece | Material | Ti-6Al-4V |
| Cutting conditions | Cutting speed, $v_c$ [m/min] | 2.5 - 7.5 |
| | Feed (uncut chip thickness), $f$ [mm] | 0.4 |
| | Width, $w$ [mm] | 2+2 |
| | Lubrication | Dry |

both workpieces clamped together during the cutting test. The validity of the set-up proposed to avoid side flow was verified after the cutting test by observing the lateral expansion using profilometer Alicona IFG4. The lateral expansion was lower than 5 $\mu$m in the constrained face whereas in the non-constrained one this expansion was higher than 20 $\mu$m.

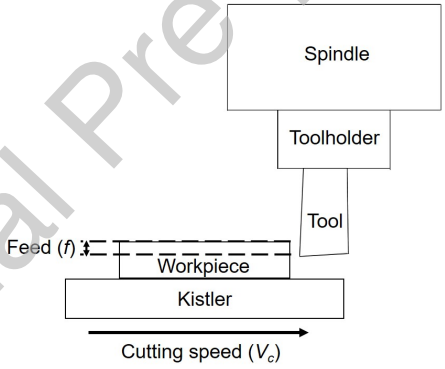


Figure 4: Scheme of the linear cutting set-up.

In order to obtain images of the deformed grid subjected to plane strain (see Figure 8), as the grid is constrained between two workpieces, the machining process was stopped suddenly during cutting and the images were obtained using the profilometer Alicona IFG4. High speed images were taken from the grid located on the front side (external grid) in order to carry out DIC measurements and to determine the state of the cut when the cutting process was stopped. This is extremely important as Ti-6Al-4V tends to create segmented chips, causing notable variations on different variables such as equivalent plastic strain or strain rate in a very short lapse of time. GOM Correlate software was employed to carry out DIC measurements. The created grid was used as speckle pattern and the quality of the pattern was ensured by the same software.

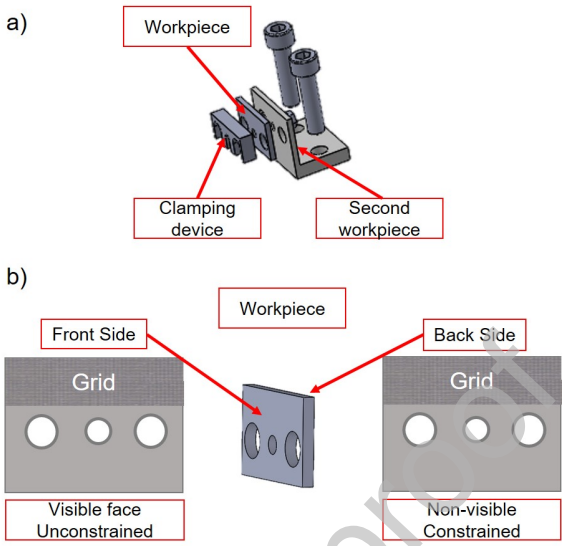


Figure 5: Scheme of the set-up to obtain plane strain conditions. a) Clamping device, workpiece and second workpiece; b) Focus on the workpiece with the grids.

As mentioned above, the material employed was the widely used aeronautical alloy Ti-6Al-4V. The material was provided as a solid hot rolled bar with a diameter of 80 mm, delivered in the annealed condition. The cutting direction was along the longitudinal direction of the bar ($Z$ direction in Figure 6). The initial microstructure of the sample was revealed with Kroll's reagent and shows a microstructure with primary $\alpha$ grains and $\alpha + \beta$ colonies oriented in the longitudinal direction. The material as received had a grain size of 10.5 ASTM and the measured microhardness was $350\text{HV}_{0.05}$.

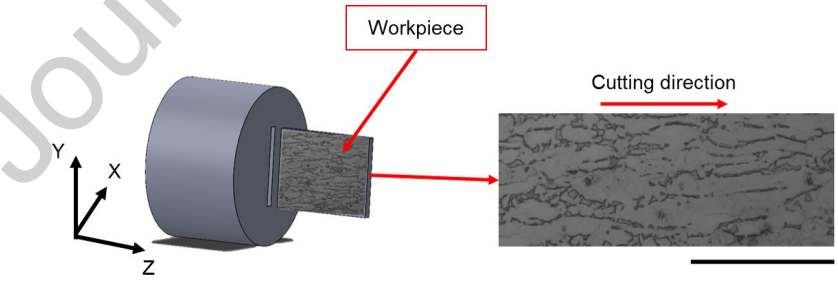


Figure 6: Scheme of the hot rolled bar to obtain the samples and initial microstructure of the Ti-6Al-4V. Scale bar: 50 $\mu$m.

The cutting speeds (see Table 1) were selected to be representative of the broaching process, widely employed to manufacture Ti-6Al-4V parts. At these

cutting speeds, the influence of the deceleration could be neglected. In addition, at these low cutting speeds, thermal effects may not be activated as stated by Zhang et al. in [14].

## 4. Results

Figure 7 shows cutting and feed forces under the cutting conditions analysed. Experimental forces showed a periodic behaviour due to chip segmentation with oscillations around 40% at the cutting speed of 2.5 m/min and 30% at the cutting speed of 7.5 m/min, in both cutting and feed forces. The oscillation period was 12 ms for the lowest cutting speed and around 4.5 ms for the highest one. A clear dependence between the oscillation frequency and the cutting speed was observed as expected. When a new cut starts, the force was minimum reaching then a maximum value just before cracking.

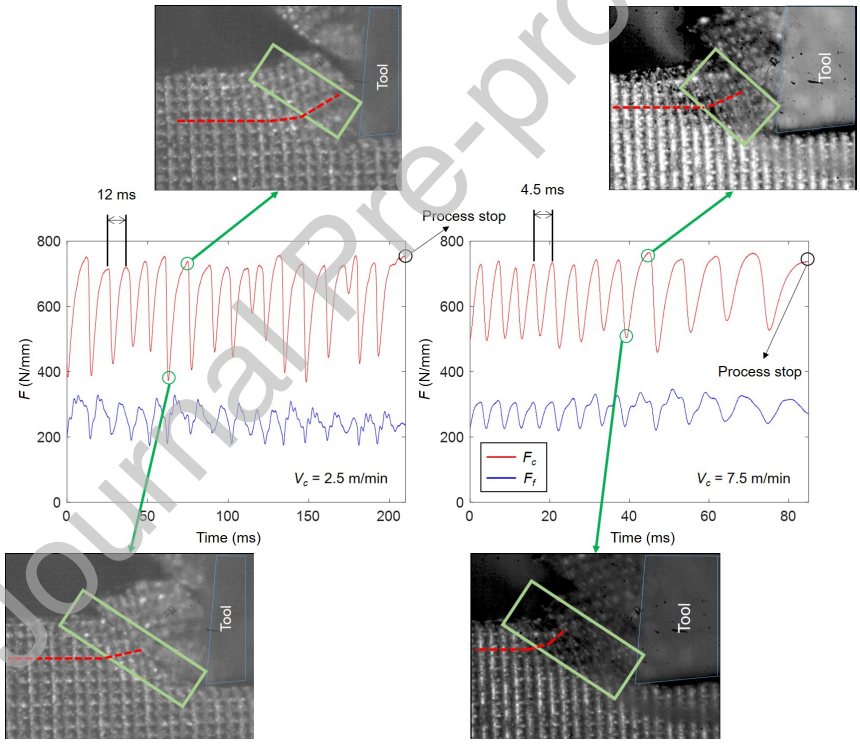


Figure 7: Experimental cutting and feed forces under the cutting conditions analyzed.

The same trend, caused by chip segmentation, is expected to be found in the rest of the variables. Therefore, it is essential to know the exact position when the cut was stopped as plastic strain and strain rate fields are expected to be notably variable during the cutting process. With regard to Figure 7,

it is possible to see that under both conditions the cutting was stopped when the cutting forces were at a maximum. In addition, it is worth noting that plastic strain and strain rate are not uniform along the shear zone taking into consideration the grid state as can be seen in Figure 7.

In Figure 7, dashed lines represent different streamlines at different points of the cutting process. It can be seen that, at the beginning of the cutting (when the cutting force is at a minimum), the streamline tends to be flatter whereas higher angles were observed when the cutting forces were at a maximum which is associated with higher deformations. Green rectangles are included to highlight this variation focusing on the shear zone at different steps of the cutting process.

Using the analytical method explained in section 2, strain rate and plastic strain were computed at 2.5 and 7.5 m/min based on the distorted grids measured with the Alicona IFG4 and shown in Figure 8. Figure 9 shows the obtained results.

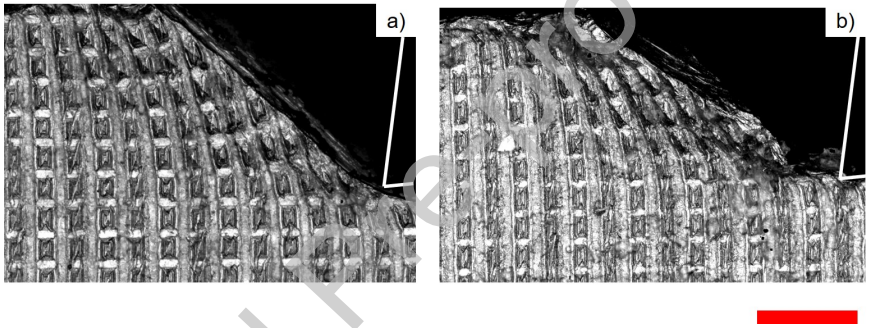


Figure 8: Deformed grid obtained after carrying out the cutting tests ($f$ = *0.4 mm*). a) Cutting speed of 2.5 m/min; b) Cutting speed of 7.5 m/min. Scale bar: 200 $\mu$m

The experimental strain rate fields, which can be seen in the Figure 9a and b, show the typical shape expected in machining: a thin layer with high values of equivalent strain rate in the primary shear zone. In the case of $v_c$ = 7.5 m/min, the plastic strain rate varies between values around 200, in the upper zone (red squares in Figure 9), and 2000 $s^{-1}$, close to the tool (red circles). In the case of $v_c$ = 2.5 m/min this variation is between 0 and 250 $s^{-1}$. The uncertainty was calculated in section 2.3, obtaining a value of 15%. The highest values are observed close to the cutting edge, especially when $v_c$ was 7.5 m/min. In addition, a notable influence of cutting speed was observed as the strain rate measured for 2.5 m/min was around 10 times lower. As it can be observed, exposed method is able to measure strain rates close to 2000 $s^{-1}$. This strain rate is, for instance, 10 times higher than the normal one reached in a compression test on a Gleeble machine [7, 10]. It is worth mentioning that such strain rates could be obtained in a SPHB test. However, using an SPHB machine, the obtained strain and heat rate are not representative of machining and, also, the load mode could be totally different [11, 12].

According to equation 6, equivalent plastic strain fields can be obtained from

equivalent strain rate fields by integrating this variable along each streamline. Results are shown in Figure 9c and d. Machining is a very aggressive mechanical process in which the equivalent plastic strain could reach values between 1 and 2 in the primary shear zone. A thin layer of high plastic strain concentration was obtained but more spread into the workpiece compared to the thin layer observed in the equivalent strain rate fields. The highest values were reached close to the tool, being around 2 at 7.5 m/min and 1 at 2.5 m/min. In the upper zone, the equivalent plastic strain was around 0.5 under both conditions. Finally, the higher the cutting speed, the higher the plastic strain was observed and the thinner the affected zone. An uncertainty of 15% was estimated with the Monte Carlo simulation.

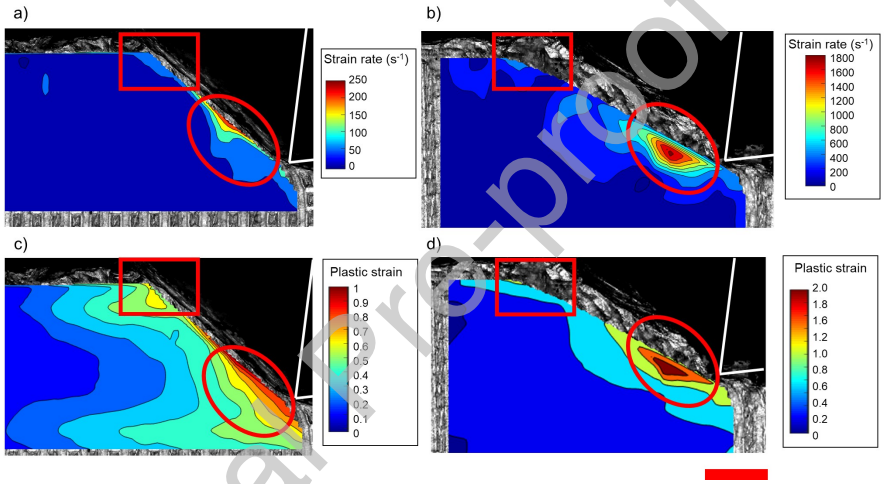


Figure 9: Experimental strain rate (a and b) and plastic strain fields (c and d) under the cutting speeds analyzed: a) $v_c = 2.5$ m/min b) $v_c = 7.5$ m/min c) $v_c = 2.5$ m/min d) $v_c = 7.5$ m/min. Tool contour is represented in white. Scale bar: 200 $\mu$m

## 5. Discussion

In order to validate the applied technique, obtained results were compared with other different techniques including experimental (DIC), analytical, literature and numerical results from a validated finite element model of the chip formation process.

### *5.1. Digital image correlation (DIC) measurements*

An attempt was made to measure the equivalent plastic strain with DIC. Because of the intense distortion expected, different subset sizes were used to generate the most accurate mesh with a step size between 1/2 and 1/3 of the subset according to [44] in order to achieve the best correlation, the following relationships between subset and step sizes were tested: 21/10, 30/12, 15/7,

21/7, 40/16 and 50/20 pixels, which are 61/29, 88/35, 44/20, 61/20, 117/47 and 146/59 $\mu$m, respectively.

The values of the plastic strain obtained with different mesh sizes suffered no variations. However, because of the extreme conditions (high strain and strain rate), notable decorrelation problems were observed, especially with low subset sizes (see Figure 10). These low subsets are not able to catch the intense distortion suffered by the pattern.

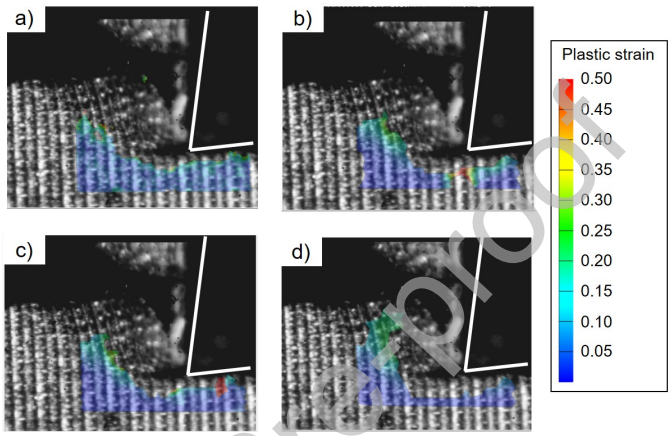


Figure 10: Equivalent plastic strain with different subset and step sizes (in pixels): a) 15/7, b) 40/16, c) 30/12, d) 50/20. Cutting conditions: $v_c = 7.5$ m/min; $f = 0.4$ mm.

In Figure 11, plastic strain results using DIC and grid method proposed are shown and compared. Both methods can only be compared in the upper zone of the shear zone, where GOM Correlate software is able to carry out the calculus. In this specific zone, the values reported by DIC method are slightly lower than the ones observed with grid method, being around 0.3 versus 0.5, respectively. Something similar happens with the strain rate, where DIC reports 300 $s^{-1}$ and grid method 500 $s^{-1}$. Similar results were obtained at 2.5 m/min.

Nevertheless, it is important to note that lower values were expected as the load mode differs notably. DIC measurements were made under conditions close to plane stress in which strains in the direction out of the shear plane are not constrained and side flow occurs. Contrary, with the grid method proposed, the measurement zone is under plane strain conditions, reducing out of plane strains. Furthermore, the existence of out of plane strains could be one of the reasons for decorrelation, due to the loss of focus, as the lateral expansion was higher than 20 $\mu$m in the non-constrained face. Therefore, the technique proposed has been proven to be able to measure plastic strain and strain rate fields under real machining conditions by overcoming typical DIC technical difficulties such as out of plane displacements which may cause loss of focus and decorrelation problems. In addition, the proposed technique allows the measurements to be made under plane strain conditions which are closer to orthogonal cutting

conditions.

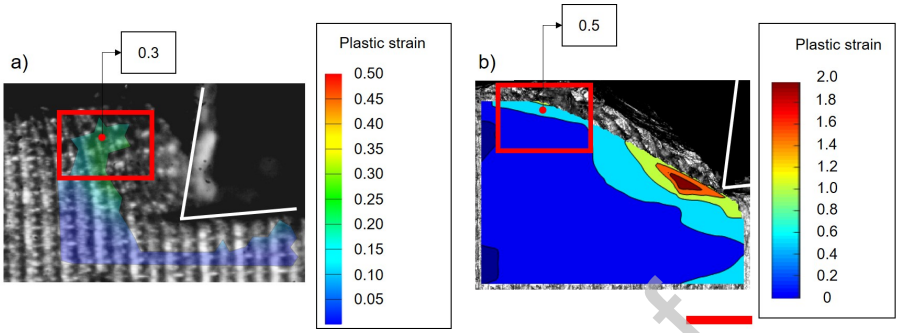


Figure 11: Equivalent plastic strain: a) DIC results, b) grid results. Cutting conditions: $v_c$ = 7.5 m/min; $f$ = 0.4 mm. Note that the scale of the colour bars is different. Scale bar: 200 $\mu$m.

### *5.2. Analytical results*

According to different authors ([38, 39]), the maximum equivalent strain rate on the shear zone for Ti-6Al-4V alloy can be calculated according to equation 8, employing the unequal division shear zone model.

$$\dot{\varepsilon}_{eq,max} = \frac{(q+1)v_c\cos(\gamma)}{\sqrt{3}t\cos(\phi-\gamma)} \tag{8}$$

where $q$ refers to the non-uniform power law distribution of velocity in the primary shear zone and can be assumed to be 3 for Ti-6Al-4V under these cutting conditions [39], $t$ is the thickness of the shear zone and $\phi$ is the shear angle. Both the thickness of the shear zone and the shear angle were measured for each cutting condition based on Figure 9, the thickness being around 0.15 mm for each condition and the shear angle 40 and 36° at 2.5 and 7.5 m/min, respectively.

Therefore, the maximum strain rate for each cutting condition calculated analytically were 753 and 2230 $s^{-1}$ for the cutting speed of 2.5 and 7.5 m/min, respectively. This implies that the trend reported by this analytical model fits with the measured experimental trend. However, the values obtained by the analytical model are higher than measured ones, especially at the lowest cutting speed. It is worth noting that the model is not able to represent the non uniformities along the shear zone in the strain rate fields.

Similarly, the equivalent strain on the shear zone can be calculated according to equation 9.

$$\varepsilon_{eq} = \frac{1}{\sqrt{3}}\left(-\frac{\sqrt{3}\dot{\varepsilon}_{eq,max}kt}{(q+1)v_c\sin(\phi)} + \frac{\cos(\gamma)}{\cos(\phi-\gamma)\sin(\phi)}\right) \tag{9}$$

where $k$ is $\frac{\sin(\phi)\sin(\phi-\gamma)}{\cos(\gamma)}$.

Under both conditions, the calculated equivalent strain was around 0.7. Therefore, the order of magnitude obtained with the analytical method and the experimental technique proposed is in agreement. The model is based on the shear angle and the thickness of the shear zone. These parameters, as it can be seen in the strain rate fields shown in [30], remain almost constant during the chip formation process, especially at the lowest cutting speed. That is why the model is not able to properly reproduce the variations on the variables because of chip segmentation. Nevertheless, it is a good tool to obtain a first notion about the order of magnitude expected in the results.

### *5.3. Literature results comparison*

Although strain and strain rate measurements under real machining conditions are still a challenge, a recent attempt was found in the literature measuring these variables in Ti-6Al-4V. Harzallah et al. [30] proposed the use of the microstructure of the material as a random speckle pattern to develop DIC measurements.

The cutting conditions analysed differ from the ones proposed in this paper. The cutting speeds were 3 and 15 m/min, for a feed of 0.25 mm. In addition, the tool geometry was also different and two different rake angles were employed being 0 and 15°. Although the proposed technique overcomes the intrinsic difficulties widely found when DIC is employed (decorrelation, loss of focus), it is worth noting that it is not able to measure under plane strain conditions, representative of the orthogonal cutting process.

Under these cutting conditions, different strain rate fields were obtained depending on the cutting state. At the highest cutting speed analysed by [30], the maximum strain rate, close to the tool, was around 5000 $s^{-1}$ for the highest rake angle, being lower for the 0 rake angle. In the upper zone these values were notably lower, similar to the results shown in Figure 9. As the cutting speed employed was twice the highest one analysed in this paper, the order of magnitude obtained is in agreement with the experimental technique proposed. Similar results were observed for the lowest cutting speed.

### *5.4. Finite Element Modelling results*

Finally, the orthogonal cutting process was simulated through AdvantEdge-2D using the model explained in [45, 46]. The employed numerical model shown in Appendix A was demonstrated to predict accurately physical relevant outcomes such as cutting forces, chip thickness, chip morphology, tool-chip contact length or shear angle. Thus, realistic values of strain and strain rate are expected. Therefore, the experimental strain and strain rates obtained using the mathematical model presented in section 2.1and based on the deformed grid shown in Figure 8, were compared with the numerical values for the different cutting conditions. Finite element simulations were able to reproduce the chip segmentation as can be seen in Figure 12.

As is shown in section 4, the cutting process was suddenly stopped when the cutting force was maximum (see Figure 7). Therefore, the corresponding frame

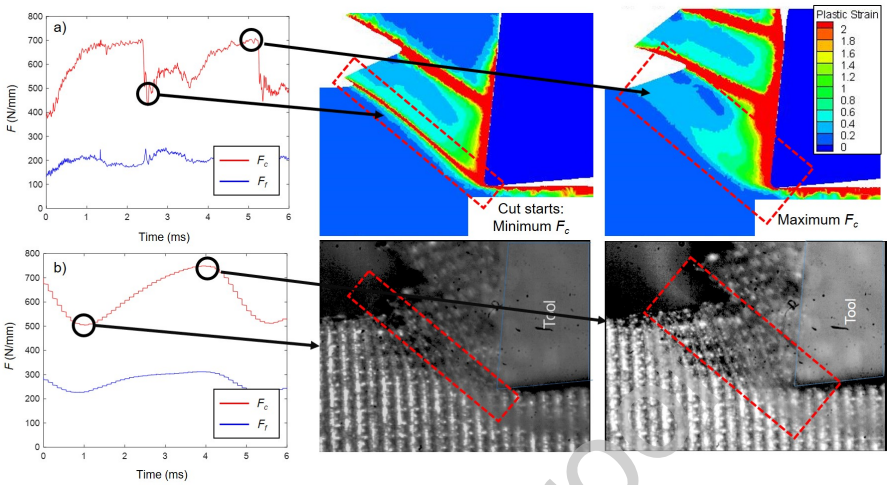


Figure 12: Plastic strain evolution on the shear zone at two different moments of the cutting process compared with experimental grids. Left: cut starts (minimum cutting force). Right: maximum cutting force. Cutting speed of 7.5 m/min. a) Finite element modelling results; b) Experimental results.

in the numerical simulations was chosen (for each condition), taking the frame at which the cutting force was maximum, in order to compare numerical and experimental results as shows Figure 13.The red square represents the upper zone of the shear zone whereas the red circle represents the zone named as close to the tool.

The numerical strain rate fields also show the typical shape expected in machining and observed by the experimental technique. In the case of $v_c$ = 7.5 m/min, the plastic strain rate oscillates between 500 $s^{-1}$ in the upper zone and a maximum value close to the tool around 1800 $s^{-1}$. In the case of $v_c$ = 2.5 m/min, as in the experimental case, this variation lies between 0 and 250 $s^{-1}$. In general, the highest values were observed close to the cutting edge for both cutting speeds. The same trend with the cutting speed was reported by the numerical model. Experimental and numerical results report the same order of magnitude. In addition, a thin layer of high plastic strain concentration was obtained with the highest values located close to the tool. At 2.5 m/min the highest plastic strain is around 1 whereas at 7.5 m/min it is around 2, in agreement with the equivalent plastic strains measured. Under both conditions, in the upper zone, an equivalent plastic strain between 0.3 and 0.5 was obtained.

## 6. Conclusions and Future work

After analyzing all the results presented above, the following conclusions can be drawn:

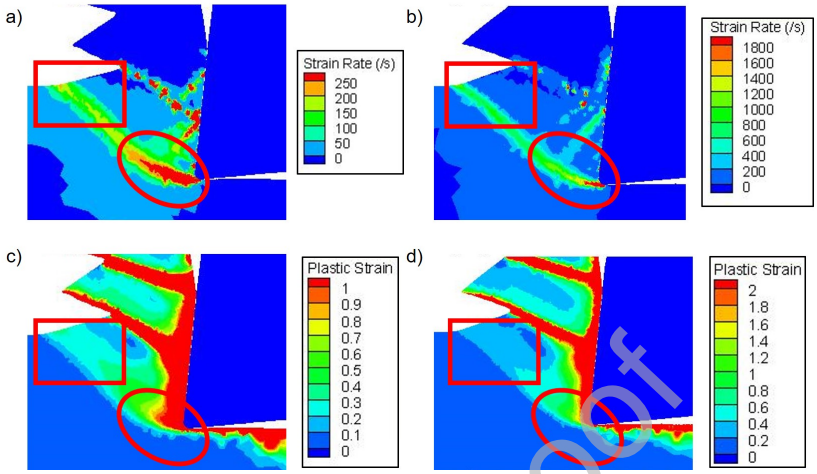


Figure 13: Numerical strain rate (a and b) and plastic strain fields (c and d) under the cutting speeds analyzed: a) $v_c = 2.5$ m/min; b) $v_c = 7.5$ m/min; c) $v_c = 2.5$ m/min; d) $v_c = 7.5$ m/min.

- It is shown that this methodology could be employed to carry out plastic strain and strain rate measurements during orthogonal cutting in realistic broaching conditions.

- With the methodology presented, equivalent strain rates of more than 1800 $s^{-1}$ and equivalent plastic strains of 2 were measured with a standard deviation of 15% computed with the Monte Carlo method, when cutting Ti-6Al-4V at 7.5 m/min with a feed of 0.4 mm.

- The proposed method allows plastic strain and strain rates to be measured using a unique image, avoiding decorrelation problems typical of DIC based methodologies and in a zone close to plane strain conditions (orthogonal cutting).In the near future the authors will try to apply the presented method to images obtained directly from a high speed camera, that would permit the analysis of time dependence of these fields. However, in such cases, conditions of plane strain would not be applicable.

- It was experimentally observed how the strain rate notably decrease when cutting speed decreases. Also equivalent plastic strain measured was lower for the lowest cutting speed.

- Experimental strain and strain rates were compared with analytical ones taking into consideration the unequal division shear zone model. The trend observed between analytical and experimental results matches well. In addition, experimental results were also compared with results presented in literature, observing the agreement between the literature results and the ones obtained with the proposed grid method. Finally, they were

compared with a finite element model, which was previously validated considering cutting forces, chip thickness, chip morphology and tool-chip contact length.

The methodology is expected to be employed at higher cutting speeds using images obtained by high speed filming, because i) at such conditions the stop methodology is not applicable, and ii) the digital image correlation software was observed to fail under these conditions. Moreover, the use of high speed images will permit the analysis of the variation of strain and strain rate as the cutting progresses, taking into account the measurement will be carried out under plane stress conditions. Obtained measurements are expected to be used as input in an objective function to carry out inverse simulation. Finally, an important issue to be implemented is the use of some kind of artificial intelligence able to select grid points to apply the method.

## Acknowledgments

The authors would like to thank the projects NG18 (KK-2018/00001), SURF-NANOCUT (RTI2018-095463-B-C21 and RTI2018-095463-B-C22), MECAERO (PIBA 2018-85) and the grant for Education and Training of Research Staff (FPU 17/02498).

The authors would like also to express our very great appreciation to Dr. Tom Childs for his valuable and constructive suggestions during the planning, development and discussion of this research work.

## References

[1] P. Arrazola, T. Özel, D. Umbrello, M. Davies, I. Jawahir, Recent advances in modelling of metal machining processes, CIRP Annals 62 (2) (2013) 695–718.

[2] P.-J. Arrazola, A. Garay, L.-M. Iriarte, M. Armendia, S. Marya, F. Le Maître, Machinability of titanium alloys (ti6al4v and ti555. 3), Journal of materials processing technology 209 (5) (2009) 2223–2230.

[3] R. M'Saoubi, D. Axinte, S. L. Soo, C. Nobel, H. Attia, G. Kappmeyer, S. Engin, W.-M. Sim, High performance cutting of advanced aerospace alloys and composite materials, CIRP Annals 64 (2) (2015) 557–580.

[4] D. Ulutan, T. Ozel, Machining induced surface integrity in titanium and nickel alloys: A review, International Journal of Machine Tools and Manufacture 51 (3) (2011) 250–280.

[5] G. Su, Z. Liu, L. Li, B. Wang, Influences of chip serration on micro-topography of machined surface in high-speed cutting, International Journal of Machine Tools and Manufacture 89 (2015) 202–207.

[6] G. Ortiz-de Zarate, A. Sela, D. Soriano, D. Soler, P. Aristimuño, P. Arrazola, Influence of chip segmentation of ti64 on the topography of the machined surface, in: AIP Conference Proceedings, Vol. 2113, AIP Publishing LLC, 2019, p. 080022.

[7] G. Germain, A. Morel, T. Braham-Bouchnak, Identification of material constitutive laws representative of machining conditions for two titanium alloys: Ti6al4v and ti555-3, Journal of Engineering Materials and Technology 135 (3) (2013) 031002.

[8] V. Tarigopula, O. S. Hopperstad, M. Langseth, A. H. Clausen, F. Hild, O.-G. Lademo, M. Eriksson, A study of large plastic deformations in dual phase steel using digital image correlation and fe analysis, Experimental Mechanics 48 (2) (2008) 181–196.

[9] A. Hor, F. Morel, J.-L. Lebrun, G. Germain, Modelling, identification and application of phenomenological constitutive laws over a large strain rate and temperature range, Mechanics of Materials 64 (2013) 91–110.

[10] M. Harzallah, T. Pottier, J. Senatore, M. Mousseigne, G. Germain, Y. Landon, Numerical and experimental investigations of ti-6al-4v chip generation and thermo-mechanical couplings in orthogonal cutting, International Journal of Mechanical Sciences 134 (2017) 189–202.

[11] J. E. Field, t. M. Walley, W. Proud, H. Goldrein, C. Siviour, Review of experimental techniques for high rate deformation and shock studies, International journal of impact engineering 30 (7) (2004) 725–775.

[12] M. Militzer, G. Botton, L.-Q. Chen, J. Howe, C. Sinclair, H. Zurob, Solid-solid phase transformations in inorganic materials 2015.

[13] A. Shrot, M. Bäker, Is it possible to identify johnson-cook law parameters from machining simulations?, International Journal of Material Forming 3 (1) (2010) 443–446.

[14] D. Zhang, X. Zhang, H. Ding, Inverse identification of material plastic constitutive parameters based on the dic determined workpiece deformation fields in orthogonal cutting, Procedia CIRP 71 (2018) 134–139.

[15] J. Pujana, P. Arrazola, R. Msaoubi, H. Chandrasekaran, Analysis of the inverse identification of constitutive equations applied in orthogonal cutting process, International Journal of Machine Tools and Manufacture 47 (14) (2007) 2153–2161.

[16] M. Daoud, W. Jomaa, J. Chatelain, A. Bouzid, A machining-based methodology to identify material constitutive law for finite element simulation, The International Journal of Advanced Manufacturing Technology 77 (9-12) (2015) 2019–2033.

[17] A. Shrot, M. Bäker, Determination of johnson–cook parameters from machining simulations, Computational Materials Science 52 (1) (2012) 298–304.

[18] F. Klocke, D. Lung, S. Buchkremer, Inverse identification of the constitutive equation of inconel 718 and aisi 1045 from fe machining simulations, Procedia Cirp 8 (2013) 212–217.

[19] R. Franchi, A. Del Prete, D. Umbrello, Inverse analysis procedure to determine flow stress and friction data for finite element modeling of machining, International Journal of Material Forming 10 (5) (2017) 685–695.

[20] X.-M. Zhang, K. Zhang, D. Zhang, J. Outeiro, H. Ding, New in situ imaging-based methodology to identify the material constitutive model coefficients in metal cutting process, Journal of Manufacturing Science and Engineering 141 (10).

[21] S.-W. Khoo, S. Karuppanan, C.-S. Tan, A review of surface deformation and strain measurement using two-dimensional digital image correlation, Metrology and Measurement Systems 23 (3) (2016) 461–480.

[22] D. Lecompte, A. Smits, S. Bossuyt, H. Sol, J. Vantomme, D. Van Hemelrijck, A. Habraken, Quality assessment of speckle patterns for digital image correlation, Optics and lasers in Engineering 44 (11) (2006) 1132–1145.

[23] B. Pan, Recent progress in digital image correlation, Experimental Mechanics 51 (7) (2011) 1223–1235.

[24] T. Baizeau, S. Campocasso, G. Fromentin, R. Besnard, Kinematic field measurements during orthogonal cutting tests via dic with double-frame camera and pulsed laser lighting, Experimental Mechanics 57 (4) (2017) 581–591.

[25] B. Thimm, J. Steden, M. Reuber, H.-J. Christ, Using digital image correlation measurements for the inverse identification of constitutive material parameters applied in metal cutting simulations, Procedia CIRP 82 (2019) 95–100.

[26] J. Outeiro, S. Campocasso, L. Denguir, G. Fromentin, V. Vignal, G. Poulachon, Experimental and numerical assessment of subsurface plastic deformation induced by ofhc copper machining, CIRP Annals 64 (1) (2015) 53–56.

[27] T. Pottier, G. Germain, M. Calamaz, A. Morel, D. Coupard, Sub-millimeter measurement of finite strains at cutting tool tip vicinity, Experimental Mechanics 54 (6) (2014) 1031–1042.

[28] Y. Guo, W. D. Compton, S. Chandrasekar, In situ analysis of flow dynamics and deformation fields in cutting and sliding of metals, Proc. R. Soc. A 471 (2178) (2015) 20150194–1–15.

[29] Y. Guo, C. Saldana, W. D. Compton, S. Chandrasekar, Controlling deformation and microstructure on machined surfaces, Acta materialia 59 (11) (2011) 4538–4547.

[30] M. Harzallah, T. Pottier, R. Gilblas, Y. Landon, M. Mousseigne, J. Senatore, Thermomechanical coupling investigation in ti-6al-4v orthogonal cutting: Experimental and numerical confrontation, International Journal of Mechanical Sciences 169 (2020) 105322.

[31] S. Jeelani, K. Ramakrishnan, Subsurface plastic deformation in machining annealed 18% ni maraging steel, Wear 81 (2) (1982) 263–273.

[32] H. Ghadbeigi, S. Bradbury, C. Pinna, J. Yates, Determination of microscale plastic strain caused by orthogonal cutting, International Journal of Machine Tools and Manufacture 48 (2) (2008) 228–235.

[33] D. Schnur, D. Lee, Determination of strain distributions in machined chips, Metallurgical Transactions A 15 (9) (1984) 1777–1779.

[34] J. Pujana, P. Arrazola, J. Villar, In-process high-speed photography applied to orthogonal turning, Journal of materials processing technology 202 (1-3) (2008) 475–485.

[35] M. Stevenson, P. Oxley, An experimental investigation of the influence of speed and scale on the strain-rate in a zone of intense plastic deformation, Proceedings of the Institution of Mechanical Engineers 184 (1) (1969) 561–576.

[36] A. J. Qureshi, J.-Y. Dantan, V. Sabri, P. Beaucaire, N. Gayton, A statistical tolerance analysis approach for over-constrained mechanism based on optimization and Monte Carlo simulation, Computer-Aided Design 44 (2) (2012) 132–142.

[37] R. G. Wilhelm, R. Hocken, H. Schwenke, Task specific uncertainty in coordinate measurement, CIRP Annals 50 (2) (2001) 553 – 563.

[38] B. Li, X. Wang, Y. Hu, C. Li, Analytical prediction of cutting forces in orthogonal cutting using unequal division shear-zone model, The International Journal of Advanced Manufacturing Technology 54 (5-8) (2011) 431–443.

[39] W. Bai, R. Sun, A. Roy, V. V. Silberschmidt, Improved analytical prediction of chip formation in orthogonal cutting of titanium alloy ti6al4v, International Journal of Mechanical Sciences 133 (2017) 357–367.

[40] C. Gáspár, Multigrid technique for biharmonic interpolation with application to dual and multiple reciprocity method, Numerical Algorithms 21 (1-4) (1999) 165–183.

[41] E. Gandarias, P. Arrazola, P. Aristimuno, R. Lizarralde, S. S. Dimov, D. T. Pham, K. Ivanov, A. Popov, Deteccion de rotura de herramientas en el microfresado mediante nuevos sistemas de monitorizado.

[42] I. ISO, Guide 98-3 (2008) uncertainty of measurementpart 3: guide to the expression of uncertainty in measurement (gum: 1995), International Organization for Standardization, Geneva.

[43] G. Ortiz-de Zarate, A. Sela, M. Saez-de Buruaga, M. Cuesta, A. Madariaga, A. Garay, P. J. Arrazola, Methodology to establish a hybrid model for prediction of cutting forces and chip thickness in orthogonal cutting condition close to broaching, The International Journal of Advanced Manufacturing Technology 101 (5-8) (2019) 1357–1374.

[44] I. D. I. C. Society, A good practices guide for digital image correlation (2018).

[45] T. H. Childs, P.-J. Arrazola, P. Aristimuno, A. Garay, I. Sacristan, Ti6al4v metal cutting chip formation experiments and modelling over a wide range of cutting speeds, Journal of Materials Processing Technology 255 (2018) 898–913.

[46] G. Ortiz-de Zarate, A. Sela, F. Ducobu, M. Saez-de Buruaga, D. Soler, T. Childs, P. Arrazola, Evaluation of different flow stress laws coupled with a physical based ductile failure criterion for the modelling of the chip formation process of ti-6al-4v under broaching conditions, Procedia CIRP 82 (2019) 65–70.

[47] T. Childs, Ductile shear failure damage modelling and predicting built-up edge in steel machining, Journal of Materials Processing Technology 213 (11) (2013) 1954–1969.

[48] A. Mondelin, F. Valiorgue, E. Feulvarch, J. Rech, M. Coret, Calibration of the insert/tool holder thermal contact resistance in stationary 3d turning, Applied Thermal Engineering 55 (1-2) (2013) 17–25.

[49] J. Rech, P. Arrazola, C. Claudin, C. Courbon, F. Pusavec, J. Kopac, Characterisation of friction and heat partition coefficients at the tool-work material interface in cutting, CIRP Annals 62 (1) (2013) 79–82.

**Declaration of interests**

The authors declare that they have no known competing financial interests or personal relationships that could have appeared to influence the work reported in this paper.

## Appendix A. Finite Element Method with AdvantEdge

In this section, a brief explanation of the numerical model employed is given including its validation taking into consideration cutting forces, tool-chip contact length and chip thickness and geometry. The chip thickness was measured using several frames of recorded video with a high speed camera, the reported values being an average of these measurements. Tool-chip contact length was measured observing the affected zone of the insert after the machining process. To avoid wear effects, a fresh tool was used for each cut. It is important to note that during machining contact length depends on the machining state, especially for segmented chips. Therefore, as this variable is experimentally measured a posteriori, the obtained contact length is the maximum one.

Simulations were carried out in AdvantEdge-2D software, which uses elasto-plastic Lagrangian code with continuous remeshing and adaptive meshing. A minimum element size of 2 $\mu$m was chosen in order to ensure the accuracy of the results. Cutting conditions and geometry are indicated in Table 1. The remeshing technique ensures the element size is minimum in the shear zone as Figure A.14 shows. The cutting tool is defined as a rigid body with rotation and translation constrained. The boundary conditions are summarized in Figure A.14.

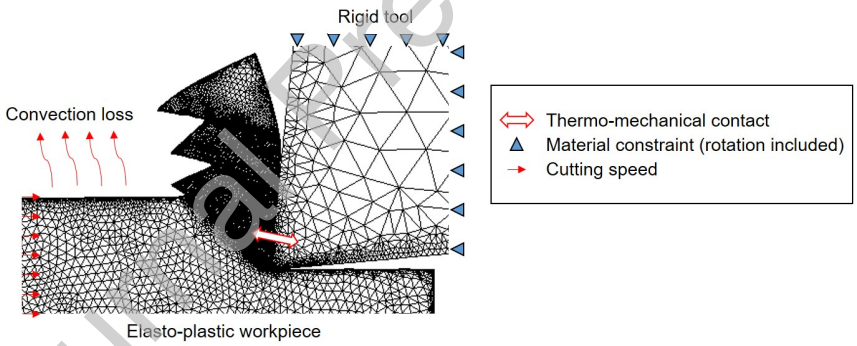


Figure A.14: Boundary conditions of the FEM model for orthogonal cutting.

With regard to the material model, one of the main input parameters is the flow stress behaviour of the material. The Johnson and Cook model was chosen, with the material parameters taken from [46]. In spite of its relative simplicity, the Johnson and Cook model considers isotropic hardening, strain rate hardening and thermal softening. The validity of this flow behaviour was previously analysed in [46] in comparison to other more complex laws and was demonstrated its capability to reproduce the machining outcomes accurately.

As mentioned before, Ti-6Al-4V tends to generate segmented chips due to lack of ductility at low cutting speeds and adiabatic shearing at high cutting speeds. To model this behaviour, it is necessary to introduce a ductile failure model. In this case, the failure model was taken from [47] as it was proved to

be valid in a wide range of cutting speeds. Both failure and flow stress models were introduced into AdvantEdge by user defined subroutines [46, 47].

The thermal conductivity and heat capacity of the material were taken from literature [48]. As shown in [45], the heat capacity of the tool material (H13A) was drastically reduced from the real physical value in order to reduce the time needed to reach thermal steady state. The sticking-sliding model was chosen to model the friction of the material, with a friction coefficient of 1 in order to ensure that most of the contact was governed by the sticking region [47, 49].

*Finite element model validation*

Cutting forces, chip thickness, shear angle and tool-chip contact length were measured from the machining tests and compared with Finite Element Method (numerical) results to show the capability of the model of reproducing the mechanics of the machining process.

*Cutting forces*

As Figure 7 shows, the peak to peak time was 4.5 ms for the highest cutting speed and, thus, a segmentation frequency of 222 Hz was obtained. Maximum and minimum average experimental cutting forces were 739 and 525 N/mm, respectively. For the feed force, these values were 304 and 225 N/mm. Carrying out the same analysis for 2.5 m/min, maximum cutting and feed forces were, 750 and 311 N/mm, respectively. The minimums were 410 and 170 N/mm. The segmentation frequency was 83.3 Hz, which is around 3 times lower than the one obtained at 7.5 m/min.

With respect to numerical results, segmentation frequency from numerical simulations was 275 Hz for the highest cutting speed and 111 Hz for the lowest one. These frequencies are slightly higher than experimental ones, but the observed trend was the same as in the experiments. Maximum and minimum numerical forces for each condition are compared with the experimental ones in Figure A.15.

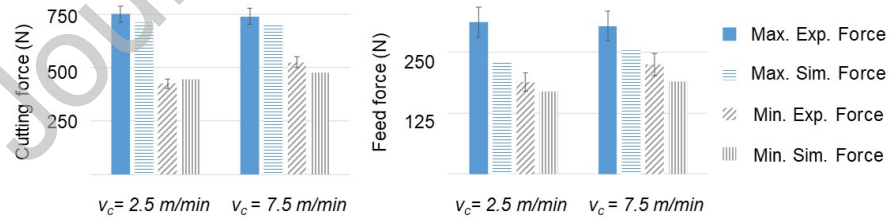


Figure A.15: Experimental and simulated cutting forces (maximum and minimum).

Cutting forces are notably well predicted, the relative error between simulated and experimental force being lower than 10%. However, there is a slight underprediction on the feed force, with a relative error close to 20%, although the trends are well predicted. This discrepancy could be assumed to be due to

an underestimation of the friction value, especially at the lowest cutting speed, at which the friction is expected to be higher. Finally, it was observed that the effect of the cutting speed on cutting forces was almost negligible. As it was mentioned in section 3, at these low cutting speeds, the thermal effects may not be activated as the temperature rise is expected to be low and also strain rate effects could be dismissed, as stated, for instance, by Zhang et al. [14].

*Chip thickness*

The oscillation observed in the machining forces (especially regarding cutting forces) is related to the segmentation of the chip. This segmentation was observed during the cutting tests and was also reproduced by the numerical model (see Figure A.16). The chip segmentation frequency was measured based on high speed images, reporting values of 220 Hz and 85 Hz, respectively.

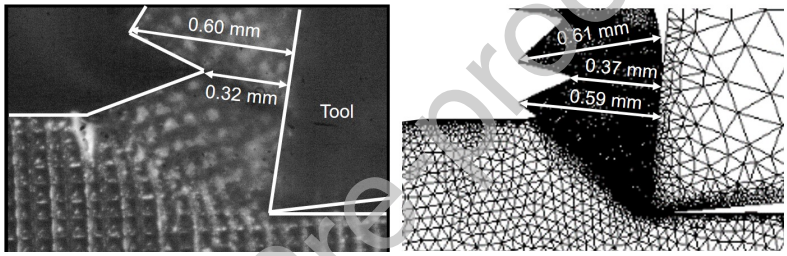


Figure A.16: Experimental (left) and simulated (right) chip geometry at 7.5 m/min. Both images are at the same scale.

Numerical and experimental chip thicknesses were observed to be in agreement. Discrepancies between them were about 50 $\mu$m (comparing, for instance, the lowest values of both pictures in Figure A.16), considering both peak and valley values. The uncertainty concerning the measurements was 50 $\mu$m for both numerical and experimental results. Results under both conditions are shown in Figure A.17, reporting agreement between experimental and simulated results. The effect of cutting speed on chip thickness was almost negligible within the studied range. In addition, the shape of the strain rate field allows the shear angle to be measured in both numerical and experimental images.The obtained values are coincident being around 40 and 36 degrees, at 2.5 and 7.5 m/min, respectively.

*Tool-chip contact length*

To obtain this parameter from the numerical model, the criterion used was the presence of force in Y direction over the rake face of the tool. In Figure A.18, experimental and numerical values are presented. In the case of numerical contact length, the edge radius effect was not taken into account. Thus, the numerical value, after adding the edge radius, was 0.57 mm. The standard deviation of contact lengths was 6% in experimental measurements and around 10% in the simulation, depending on the selected frame.

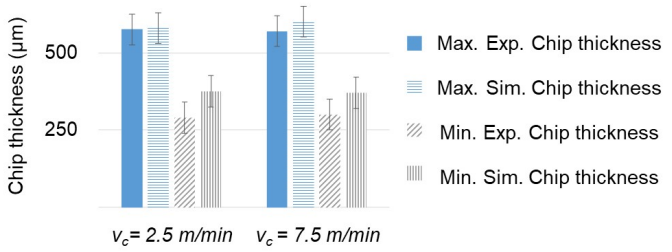


Figure A.17: Experimental and simulated chip thickness (maximum and minimum).

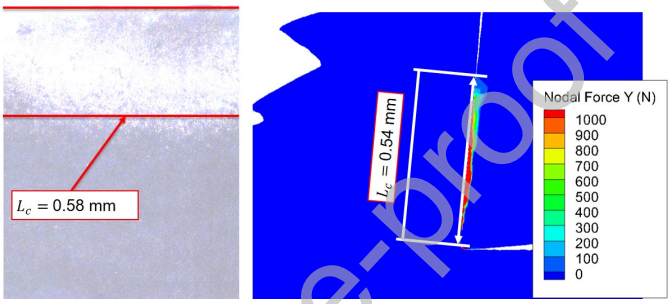


Figure A.18: Experimental (left) and simulated (right) tool-chip contact length at 7.5 m/min.

Figure A.19 shows the numerical and experimental contact length for both cutting speeds observing errors in the prediction lower than 2%. There was a slight decrease in the contact length with cutting speed considering both experimental and numerical results.

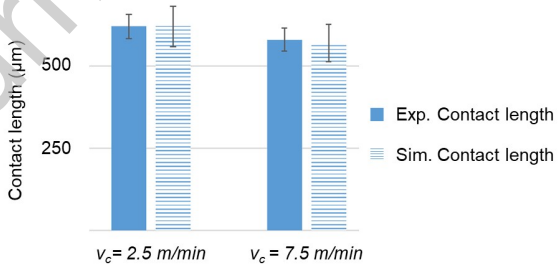


Figure A.19: Experimental and simulated tool-chip contact lengths.

**Autorship contribution**

**Andrés Sela:** Conceptualization, Methodology, Formal analysis, Investigation, Writing-Original draft.

**Gorka Ortiz-de-Zarate:** Methodology, Software.

**Daniel Soler:** Conceptualization, Methodology, Software, Validation, Writing- Original draft, Formal analysis.

**Guénaël Germain:** Writing-Review & Editing, Supervision.

**Patxi Aristimuño:** Methodology, Investigation, Resources.

**Pedro-J Arrazola**: Conceptualization, Writing-Review & Editing, Supervision, Validation, Project administration, Funding acquisition.